coatings

MDPI

Article

The Influence of NIR Pigments on Coil Coatings' Thermal Behaviors

Stefano Rossi *, Massimo Calovi, Domenico Dalpiaz and Michele Fedel

Department of Industrial Engineering, University of Trento, Via Sommarive 9, 38123 Trento, Italy; massimo.calovi@unitn.it (M.C.); domenico.dalpiaz@gmail.com (D.D.); michele.fedel@unitn.it (M.F.)
* Correspondence: stefano.rossi@unitn.it; Tel.: +39-0461-282442

Received: 2 May 2020; Accepted: 26 May 2020; Published: 28 May 2020

Abstract: The effect of over-heating in urban areas, called the urban heat island effect (UHI effect), is responsible for greater energy consumption for cooling buildings. Several reflective near-infrared (NIR) coatings, called cool coatings have proved to be effective for contrasting the UHI effect. The thermal and appearance properties of cool coatings depend on the color and they often have been studied only at the initial state, without undergoing atmospheric degradation and soiling. In this work, the thermal, visual and durability behaviors of red and brown polyester-based organic coatings for roof applications were studied. All samples were subjected to accelerated degradation cycles composed of UV-B and salt spray chamber exposure. The sample degradation was assessed by infrared spectroscopy, gloss and colorimetric analyses. Moreover, the thermal behavior was studied by means of a simplified experimental setup. Finally, a soiling and weathering test was conducted to simulate the soiling of three years' external exposure. Despite the phenomena of chemical degradation and a decrease in aesthetic properties, the samples maintain their thermal performance, which is not even influenced by dirt products. In addition, NIR pigments significantly improve the thermal behavior of brown coatings.

Keywords: roof coating; thermal behavior; coil coatings; NIR pigments; accelerated degradation cycles; soiling

1. Introduction

Buildings are responsible for approximately 40% of energy consumption and 36% of CO_2 emissions in the EU [1]. The increasing population in cities and the consequent expansion of urban areas has led to a worsening in the so-called urban heat island effect (UHI effect) [2,3]. The term describes built-up areas that are hotter than nearby rural areas. The annual average air temperature of big cities (with one million people or more) can be up to 3 °C warmer than the nearby rural areas during the daytime. During the evening, when the sun has set, this difference expands to even 12 °C [4]. The heat that is stored during the day by buildings, roads and other construction is re-emitted slowly after sunset, creating significant temperature differences between the city and the rural surroundings where the heat escapes more rapidly [5–7].

The reasons for the UHI effect are due to different factors, the most important of which are [8]:

- Geometry of buildings that reduce the long-wave radiation loss from street canyons. Urban constructions replace the cold sky hemisphere radiating back an even greater amount of radiations.
- Usage of high absorbing materials such as concrete, asphalt and coated metal sheets. Furthermore, the replacement of natural soil in urban areas led to heat accumulation because the heat cannot be drained by evapotranspiration as instead happens in rural areas.
- Anthropogenic heat released by combustion and by animal metabolism.
- The urban greenhouse effects.
- The reduction of evaporating surfaces led to an increase in sensible heat instead of latent heat.

Heat islands can affect communities by increasing summertime peak energy demand [9], air conditioning costs, air pollution and greenhouse gas emissions, heat-related illness and mortality [4]. Urban warming has a serious impact on the energy consumption of urban buildings by increasing the energy and the electric power necessary for cooling needs. In parallel, higher ambient urban temperatures increase the concentration of certain pollutants like tropospheric ozone, deteriorate thermal comfort conditions in cities, exacerbate health and indoor environmental problems and result in a serious increase in the global ecological footprint of the cities [10]. Santamouris et al. [11] have observed that the peak energy demand per degree of temperature may rise between 0.5% and 8.5%. The threshold ambient temperature over which the electricity consumption starts to increase is for most of the cases around 18 °C.

The potential increase in the peak electricity demand triggered by ambient warming is also high. Existing studies show that the peak electricity demand increases from 0.45% to 4.6% per degree of ambient temperature rise. This corresponds to a penalty of about 21 ± 10.4 W per degree of temperature rise per person [11].

The rising energy costs and the increasing energy consumption, together with increased environmental awareness, has led to focused research on developing different strategies for contrasting the UHI effect.

Infrastructures play a fundamental role in urban temperatures [7,12–16]. The development of green areas, both vertical and horizontal, the use of materials with high albedo (the portion of the incident radiation that is reflected by a surface) and the intelligent layout of buildings to promote ventilation are strategies that have been found useful to mitigate the UHI effect.

A very common way to increase the albedo of a coating is to use light color pigment in order to increase the reflectivity in the visible part of the solar radiation. Coatings containing rutile (TiO_2) white pigment are the most effective because they have high reflectance both in the visible and in the near-infrared (NIR) range [17]. However, their color is not suitable for many applications, especially for roofs. Alternatively, since 55% of the solar power arrives on the surface of the earth in the form of infrared radiation, NIR-reflective pigments are inserted into organic coatings. In this way, a reduction of the heat absorbed by the coating is obtained without modifying its aesthetic properties [18,19]. The real effectiveness of these paints, however, depends a lot on their color. These are called "cool coatings" since they show a high thermal emittance which induces a fast heat release to the surrounding environment. Cool coatings, also for roof applications, have been widely studied [7,20–31].

However, cool coatings have to face several issues related to degradation phenomena due to dangerous atmospheric agents. Among the different weathering agents, the incoming UV-B radiation is recognized to affect and alter the aesthetical properties of many polymeric matrices, thus decreasing the functional and aesthetical properties of the coatings [32,33]. Therefore, nowadays the studies focused on roof coatings mainly deal with the maintenance of the protective, as well as thermal, performance of the polymer layers, as a function of exposure to aggressive environments and or aging agents.

This work focuses on the study of high albedo commercial coatings for roof applications produced by means of coil coating and their degradation and soiling exposure. Coil coating is a high efficiency and cost-effective production technique that allows metal coils to be painted very quickly. The semifinished products such as steel and aluminum strips are painted inline in the industrial

plant, significantly reducing the production time and costs, maintaining high quality. The reproducibility of the manufacturing process, the relatively low cost and the reduced environmental impact have contributed to increasing the use of the coil coating process [34–36]. Carbon steel and aluminum are the main substrates employed in these processes. In the case of steel, in order to ensure better weathering performance, an inline galvanization of the sheet is foreseen before painting. Furthermore, in recent years an improvement in aesthetic aspects has been achieved with the development of a very large color palette, with the possibility of having surface texturizations and different gloss levels. These aspects have led to an increase in the use of coil coatings in many industrial fields [37–40]. Coil coatings are widely used in the construction field, both for walls, facades and roofs. They can be applied both directly as coils, and as an external and protective part of building panels, where reduced building time, low cost and ease of maintenance are required [41]. The literature offers some articles that are devoted to the behavior of these products in a natural environment [42–44]. For these applications, particular colors and textures have also been developed in order to reflect the traditional finishes in bricks and tiles so as not to entail aesthetic problems or urban and building regulations issues.

Nowadays, the need to develop more and more durable coatings and the increasing attention of the building market to energy saving and efficiency issues, triggered the development of coil coatings with NIR pigments to be used to mitigate the heat absorbed by buildings. This represents a very important aspect since sheet metal roofs have significantly higher heat transmission values than traditional roofs that use ceramic materials such as cement, tiles, bricks or wood, which could lead to possible users not considering the use of coil coatings in many applications. It is, therefore, significant to understand whether the use of NIR pigments in coil products can improve their thermal performance by justifying an increase in the cost of the coil product.

This work, therefore, aims to study coil coatings that use paints with NIR pigments compared with traditional products trying to employ procedures that can simulate the real application of the coil material. Thinking about the use of these products painted as roofs, the two colors that are most used in the field of housing coverings have been identified. Red and brown commercial coatings containing NIR pigments have been characterized in this study. The cross-section and NIR pigments distribution were studied by means of scanning electron microscopy (SEM) observations. The variation of thermal efficiency, aesthetic properties and coating degradation were subsequently analyzed as a function of artificial cycles composed of artificial UV-B light and salt spray chamber exposure. Finally, the soiling effect on the coatings' thermal behavior was assessed. The two coatings were compared with their respective standard layers, free of NIR pigments. Due to this study it was, therefore, possible to verify the effect of NIR pigments and the color of the polymer matrix on the performance of layers used as roof coatings.

2. Materials and Methods

2.1. Sample Preparation

A hot-dip galvanized low carbon steel substrate for coil coating was used as a small-scale roof panel. Hot-dip galvanized steel panels (supplied by Marcegaglia Carbon Steel (Ravenna, Italy)) were degreased with an alkaline detergent (Condorine SG 503 AL) and pretreated with a chemical conversion process based on complex oxide (Condorcoat NB 100) [45]. After, the treatment with Condorcoat NB 100 the material was rinsed with tap water, demineralized water and finally sent to a further final passivation step performed with a passivating agent based on inorganic zirconium and fluorinated salts (Condorcoat EC 900) [46]. The passivation layer that is created on the surface of the material aims at providing adhesion of the paint film. After the passivation processes, the sheets were coated with a polyester-based primer. The primer was cured in a gas-fired oven, reaching a peak metal temperature (PMT) of 250 °C, and cooled down in water. Coated metal sheets were captured just before the application of the topcoat. The application of the topcoat was performed due to the use of a wire-wound coating bar, also known as a draw-down bar. The advantage of using such a bar (compared, for example, to simply drawing down with a palette knife) is that a prespecified amount

of wet paint is laid evenly on the substrate producing films of repeatable thickness [47]. Depending on the width and depth of the grooves on the bar, different film thicknesses can be achieved. The samples were produced with a wire-wound rod to obtain a wet film thickness of 36 μm. The curing of the paint was conducted in an electric oven with a revolving plate (Aalborg company, Orangeburg, NY, USA) at 350 °C for 19 s to obtain a peak metal temperature of about 220 °C. Subsequently, the samples were removed and cooled down in a water bath for 20 s and finally dried with a compressed air gun. All the samples measure 210 mm × 130 mm with a thickness of 0.5 mm. As shown in Table 1, two different color topcoats were provided by Isva Vernici Srl (Torino, Italy): brown and red colors correspond to RAL 8017 (Chocolate brown) and RAL 3009 (Oxide red) [48,49], respectively, which are the most popular colors for roof applications.

Moreover, the samples were compared with standard coating for roof applications, free of NIR pigments, in order to study the effect of these fillers.

Table 1. Coatings color, with relative nomenclature.

Sample Nomenclature	Pigments	RAL Code
Red	standard	3009
Red-N	NIR	3009
Brown	standard	8017
Brown-N	NIR	8017

The chemical nature of the pigments is described in Table 2, provided by the supplier and confirmed by EDS measurements. The values shown in the table are normalized, without considering the carbon and oxygen elements, which represent the major constituents of the polymer matrix and consequently would have altered the results of the analysis on the pigments.

Table 2. Normalized mass in percentage (%) of elements in the samples. A high content of carbon and oxygen are obviously found (not reported), coming from the polymeric nature of the binder.

Element	Red	Red-N	Brown	Brown-N
Si	8.86 ± 0.28	9.65 ± 0.22	10.69 ± 0.64	8.96 ± 0.52
Ti	12.95 ± 0.28	10.95 ± 0.18	9.42 ± 0.38	5.30 ± 0.24
Fe	35.34 ± 0.63	65.08 ± 0.92	55.73 ± 1.92	55.58 ± 1.86
Zn	33.49 ± 0.62	39.21 ± 0.92	13.33 ± 0.54	12.39 ± 0.50
Cr	-	-	-	11.36 ± 0.44
Ca	-	-	-	0.64 ± 0.08

Regarding the red coatings, the product containing the NIR-reflective pigments possesses a greater concentration of iron respect to the Red standard layer. In fact, iron oxide (Fe_2O_3) is widely used as a red pigment and it is considered also a NIR-reflective pigment [50]. The higher content of iron oxide should enhance the reflectivity in the IR range due to the increased opacity to IR [51]. On the other hand, the NIR pigments in the brown products contain chromium, another element used to increase the reflectivity in the IR range [51]. Otherwise, there are no major differences between the elementary analysis of the two brown topcoats.

2.2. Characterization Techniques

The thicknesses of the different coatings were measured with the Phynix Surfix digital thickness gauge (Neuss, Germany). The surface morphology and pigment distributions were investigated with a low-vacuum SEM (JEOL IT 300, Akishima, Tokyo, Japan).

All the samples were, therefore, subjected to 4 cycles of accelerated degradation. Each accelerated degradation cycle was composed as follows:

- Seven days (168 h) of UV-B exposure in an irradiation chamber in accordance with the ASTM-G154-06 standard [52] using a fluorescent light source (UV-B 312-EL Hg lamp) with an irradiated power of 600 W/m^2. The total amount of UV-B exposure was set to 672 h.
- Seven days (168 h) of salt spray in an Ascott CC IP salt spray chamber, following the ASTM B117/18 standard [53]. The total amount of salt spray exposure was set to 672 h.

During exposure to degradation cycles, the edges of the samples were not protected, in order to simulate the real behavior of the material in roof coatings applications.

After each degradation cycle all the samples were characterized by measuring their thermal performance as well as their appearance properties. The surface modifications upon exposure in the aging cabinets were studied by means of FTIR, gloss and colorimetric analyses. The FTIR spectra were acquired by performing an FTIR spectroscopy (Varian 4100 FTIR Excalibur spectrometer, Santa Clara, CA, USA) on each sample to assess the chemical modifications of the polymeric matrix. Five gloss measures were performed for each sample in accordance with the ASTM D523/14 (2018) [54] standard with an Erichsen 503 instrument. The geometry at 60° was exploited because it is the most appropriate for medium gloss organic coating. A Konica Minolta CM-2600d spectrophotometer (Chiyoda-ku, Tokyo, Japan) was employed for the colorimetric analyses. The data were collected using a D64 illuminant with an observer angle of 10° and an aperture diameter of 10 mm. These measurements were done in accordance with the CIELab color space method [55].

For each coating sample, three color measurements at three different positions on the surface were collected. The data were represented as the arithmetic mean of the obtained data points.

The organic coating's thermal behavior was assessed employing the experimental setup depicted in Figure 1. The samples under investigation are located as roof panels on a small-scale polystyrene foam (XPS) made a house model with a plane roof. Each coating sample was subjected to a 150 W IR-emitting lamp (Philips IR150R R125, Eindhoven, Netherlands) placed 26 cm above the samples.

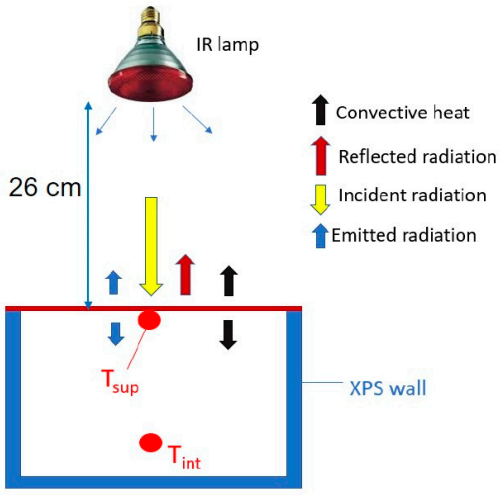

Figure 1. Schematic description of the small-scale houses utilized as support for the roof panels for thermal measurements. The red dots represent the thermocouples that were attached behind the metal sheet and inside the house models at 4 cm from the floor. The thermocouples were connected to a data logger.

Two thermocouples PT 100 were located on the rear surface of the metal sheet on the bottom of the small-scale houses. A Delta OHM HD 32.7 RTD data logger was employed to collect the temperature values (sampling: one per minute) for about 35 min after switching on the lamp and an

additional 25 min after the lamp was switched off. These timings were necessary in order to achieve a constant temperature called Plateau Temperature ($T_{plateau}$). In this work, the $T_{plateau,sup}$ and $T_{plateau,int}$ are the temperatures reached at 1620 s (27 min) by the lower face of the samples and by the thermocouple within the small-scale house, respectively. The distribution of the temperatures on the frontal surface of the roofs panel was monitored by using a Geo Fennel FTI 300 thermal imaging camera (Baunatal, Germany).

Further tests for investigating the surface wettability were conducted at the initial state and after the fourth degradation cycle. The tests were performed following the ASTM D7334/08 [56] standard practice. A Nikon 60 mm lens f/2.8 for macro pictures was used and the wetting angle was measured by using the NIS-Elements Microscope Imaging software (Windows Version). The drops were formed with a syringe and dropped from a height of about 2 cm. Once the drop was focused the picture was captured, the wetting angle was measured by means of the imaging software. Six measurements were performed for each sample to obtain statistical validity.

Finally, the accelerated test for the soiling and weathering of the samples was carried out in accordance with the ASTM D7897/18 [57] standard practice. This new standard has been specially developed for the soiling and weathering of roofing materials, simulating 3 years of field exposure. An aqueous mixture of 4 soiling agents, specifically selected for simulating the natural soiling due to dust, living vegetation and smog, was sprayed on the sample. The soiling mixture is composed of the following agents:

- Dust: a mixture of 0.3 g iron oxide Fe_2O_3 powder (CAS 1309-37-1), 1.0 g of montmorillonite K_{10} powder and 1.0 g of bentonite, transferred to 1 L of distilled water (suspension of 2.3 g/L).
- Salts: a mixture of 0.3 g of sodium chloride NaCl, 0.3 g of sodium nitrate $NaNO_3$ and 0.4 g of calcium sulfate dihydrate $CaSO_4$ $2H_2O$, transferred to 1 L of distilled water (solution of 1.0 g/L).
- Particulate organic matter (POM): 1.4 g of humic acid (CAS 1415-93-6) diluted in 1 L of distilled water (solution of 1.4 g/L).
- Soot: 0.26 g of carbon black (Vulcan XC-72) diluted in 1 L of distilled water (solution of 0.26 g/L).

Following the standard, this composition of the soiling mixture simulates the Miami climate. This composition was chosen because it contains higher soot and humic acid content. In fact, the soot is the main responsible for the drop in thermal properties. The test sample is prepared in three stages:

- Weathering: apparatus exposure before soiling: 2 cycles, each of them composed of 8 h in UV-A chamber and 4 h of water condensation at 50 °C and a final dry under the infrared lamp;
- Soiling: spray the mix of dust, salts, organic matter and soot and dry under the infrared lamp;
- Weathering: apparatus exposure after soiling: 2 cycles, each of them composed of 8 h in UV-A chamber and 4 h of water condensation at 50 °C and a final dry under the infrared lamp.

The water condensation was performed in an Erichsen Hygrotherm 519 SA humidostatic chamber (Erichsen, Hemer, Germany). The soiling mixture was sprayed, placed 30 cm above the sample, until the wet soiling mass was 8 ± 1 mg/cm^2. The samples were dried under a 150 W IR-emitting lamp (Philips IR150R R125) for 15 min. After the drying each sample was covered with randomly distributed soil spots with a diameter ranging between 1 and 3 mm as prescribed in the standard. The thermal properties were evaluated after the soiling and weathering procedure for all the samples. Therefore, the samples were gently cleaned under tap warm water to remove all the impurities and dirt. After the cleaning process the thermal properties were re-evaluated to exploit the differences. The detailed procedure is described in the ASTM D7897/18 [57] standard practice.

3. Results and Discussion

3.1. Pigment Recognition and Coatings Defects

The protective system thickness was measured with the thickness gauge (see Table 3).

Table 3. Total thickness of the protective system (topcoat + primer).

Sample Nomenclature	Thickness (μm)
Red	25.9 ± 1.9
Red-N	25.0 ± 2.0
Brown	24.4 ± 2.2
Brown-N	26.2 ± 3.1

The data shown in Table 3 are the result of the average of five measurements per sample, carried out on five samples for each type of coating (25 measurements in total). The four series of coatings have comparable dimensions: their different properties and performances are, therefore, not influenced by different thicknesses of the protective layer.

However, the data obtained by the thickness gauge represent the sum of the thicknesses of the primer and the topcoat. In order to differentiate the dimensions of these two layers, the samples were, therefore, studied in cross-section through SEM observation. Figure 2 shows the section of the Brown sample: in addition to the topcoat and the primer, the zinc layer formed following the hot-dip galvanizing process is observable. The thickness of the topcoat is approximately 20 μm, while the zinc layer possesses thicknesses comparable with the primer, slightly greater than 6 μm. These values of thickness are comparable for all types of samples being studied.

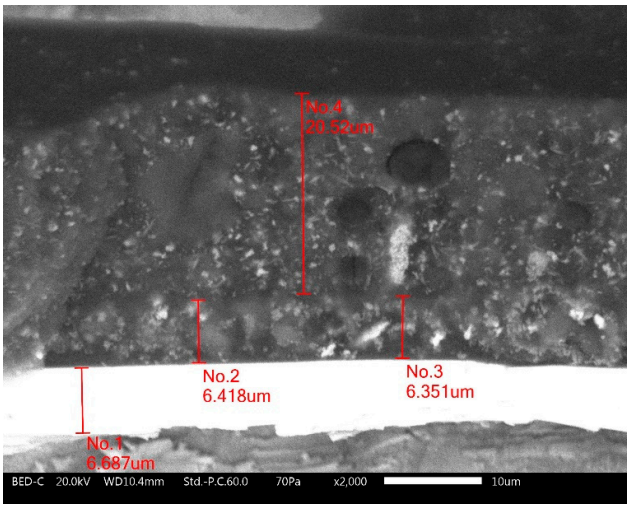

Figure 2. SEM cross-section image of sample Brown. From the bottom: the white layer represents the zinc layer, above which there is the primer, about 6 μm thick, and finally the topcoat.

Consequently, the samples observed at SEM were also analyzed by EDS techniques, to assess the dispersion of the pigments in the polymeric matrix. In Figure 3, it is possible to observe the SEM images of the red samples at different magnifications.

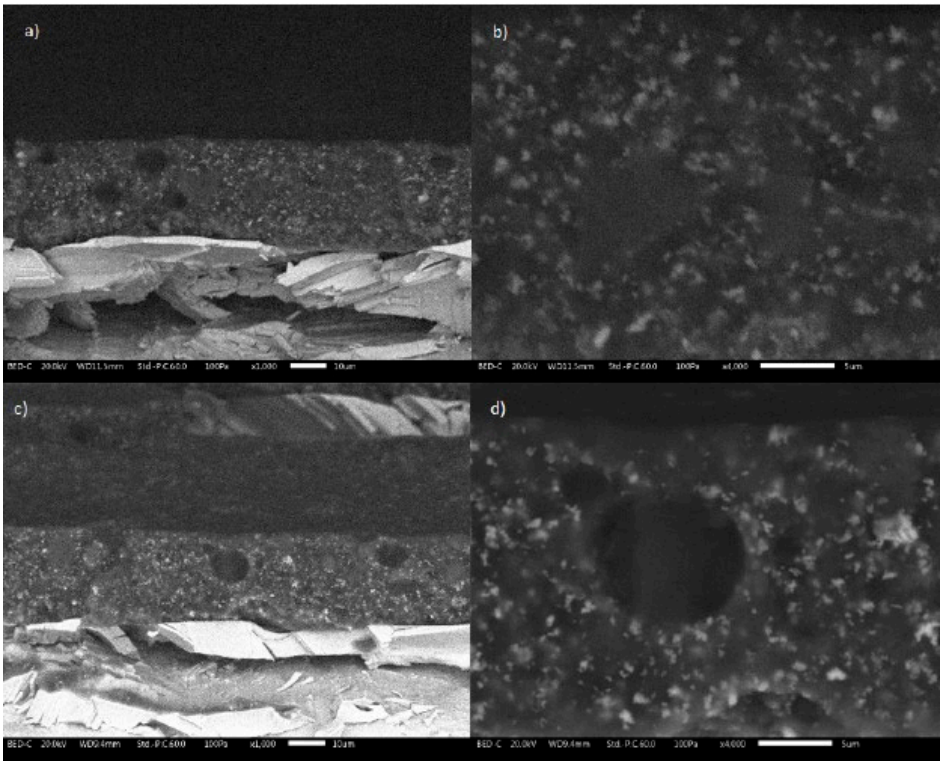

Figure 3. SEM images of red samples. (**a**,**b**) Images of the Red sample at increasing magnifications. (**c**,**d**) Images of the Red-N sample at increasing magnifications.

The pigment dispersion is uniform, while their dimensions vary between 1 and 2 μm. Moreover, some pores are observed: these bubbles are up to 5 μm large. They can be due to the fast curing process used in the coil coating production: the curing and evaporation of solvents in paints take place very quickly (less than 30 s). In the layers closed to the surface, the solvents evaporate very quickly and undergo very rapid cross-linking. Sometimes, it could happen that the underlying solvents are not able to evaporate and then they remain trapped in the coating under the cross-linked external layer. A bubble occurs when the solvent vapor seeps through the paint film skin without causing it to rupture [58]. In this case, the porosity does not affect the appearance of the coating because it does not warp the coating surface. On the other side, this defectiveness could affect the protective behavior of the organic coating, reducing the barrier effect. The appearance of the red and brown samples is the same.

3.2. Coatings Degradation

3.2.1. Changes in Chemical Structure

FTIR spectroscopy measurements were conducted on each sample at the initial state and after each UV-B/salt spray chamber degradation cycle. FTIR is very useful for monitoring the chemical and structural changes in the coatings during the degradation cycle.

Figure 4 shows the evolution of the FTIR spectra of the four samples, as a consequence of the degradation cycles, while Table 4 summarizes the main peaks assigned to the functional group.

No particular differences are observed among the four samples, according to the similar chemical nature of the binder. The only differences probably lie in the additives and pigments that are not detected with the FTIR analysis (the corresponding contributions are hidden by the intense absorption peaks of the polymeric matrix).

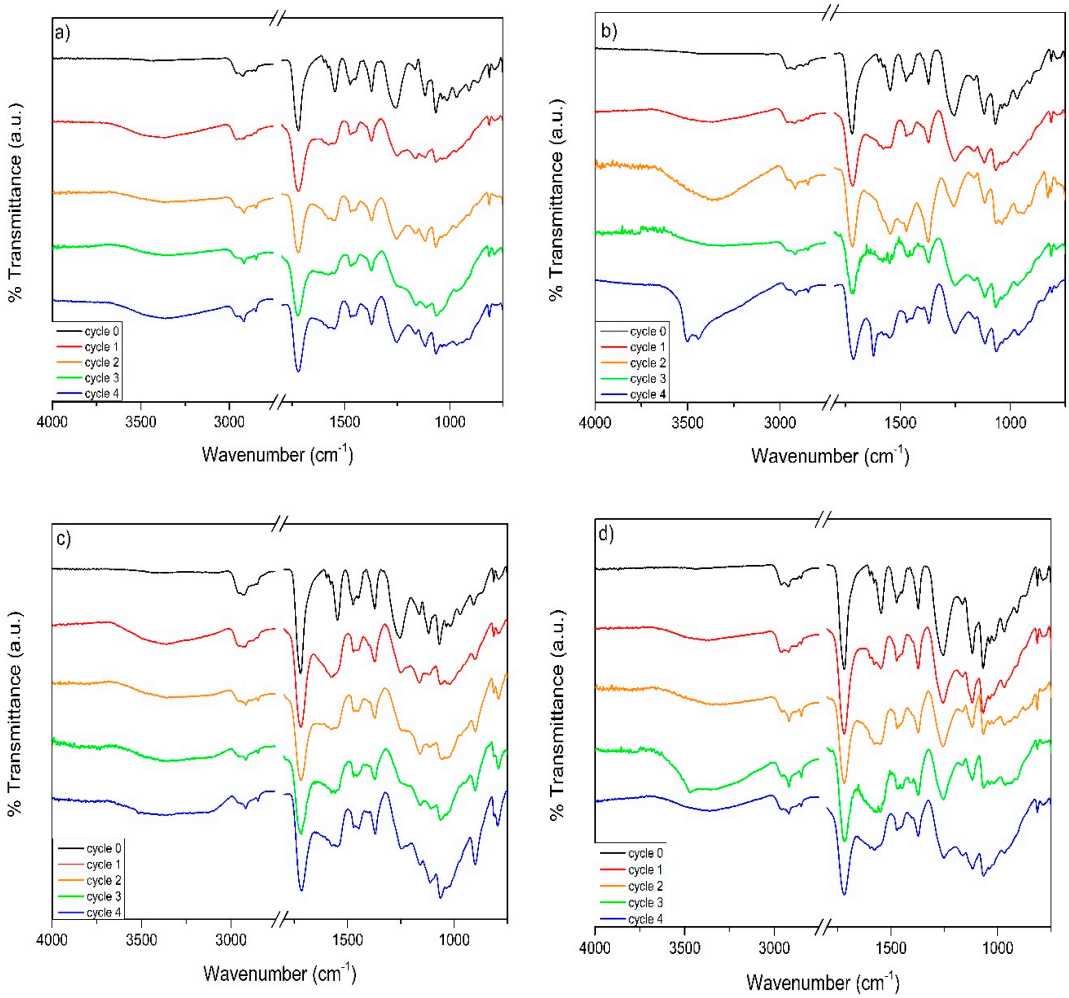

Figure 4. FTIR spectra of (**a**) sample Red, (**b**) sample Red-N, (**c**) sample Brown and (**d**) sample Brown-N as a function of the degradation cycles.

Table 4. Main IR transmission bands of analytical interest identified for all the samples.

Peak (cm^{-1})	Functional Group Assignment
989, 1071, 1475	bending C=O
1160,1105	C-O-C aliphatic ester
1240	C–O
1375	bending CH_3
1388, 1475	bending CH_2 aliphatic
1720	stretching C=O
2870	stretching CH–
2970	stretching CH_2–

Taking the sample Red as an example, a general broadening of the peaks is observed (Figure 4a) with the accelerated aging cycles. Notice, in particular, the peak at 1720 cm^{-1} associated with the C=O group. The general broadening can be due to the degradation of the polymeric binder and to the surfacing of pigments on the surface, called chalking. The extent of degradation of the investigated materials was evaluated based on the methodology presented by Gerlock et al. [59], who studied the degradation of melamine coating, monitoring the photooxidation intensity by the disappearance of the CHn band and appearance of OH and NH bands. The degradation process was monitored in terms of photooxidation index (POI), which is defined as follows [60]:

$$\text{POI} = \frac{\text{Rabs[OH/CH]}t}{\text{Rabs[OH/CH]0}} \quad (1)$$

where Rabs[OH/CH]0 is the ratio between the peak's height at 3400 cm^{-1} associated to the OH group and the peak at 2970 cm^{-1} associated to the CH_2 at the initial state, while Rabs[OH/CH]t is the same ratio but after a certain degradation. The peak at 3400 cm^{-1} was not observed in the samples at the initial stage but appears bigger and bigger as the degradation increases.

Figure 5 shows the evolution of the POI value as a function of the degradation cycles. The POI increases very steeply after the first degradation cycle and then it tends to stabilize. The NIR pigments seem to slightly promote photooxidation phenomena, especially in the fourth degradation cycle, both for coating Red-N and coating Brown-N. In general, brown coatings suffer most from these degradation cycles, with slightly higher POI values than their respective red layers.

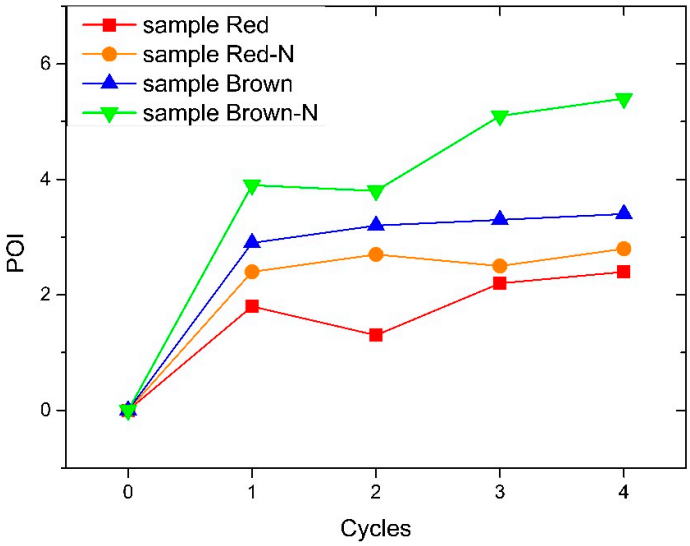

Figure 5. Photooxidative index photooxidation index (POI) as a function of the degradation cycles.

3.2.2. Visual and Aesthetical Evaluation

Chemical degradation phenomena are often associated with a variation in the aesthetic performance of the product. The samples were, therefore, subjected to color and gloss measurements, to verify their change as a consequence of the degradation cycles.

Table 5 summarizes the gloss values of the four coatings before exposure to degradation cycles.

Table 5. Initial state gloss measurements at 60° for all the samples.

Sample	Gloss (GU)
Red	31.8 ± 0.1
Red-N	31.2 ± 0.1
Brown	37.5 ± 0.2
Brown-N	31.7 ± 0.2

The loss of gloss was used to follow the surface features' evolution of the samples. In fact, when a pigmented film degrades, the surface gradually roughens due to the body of the binder being lost, with a consequent loss of gloss. The particles of the pigments remain upon the surface in the form of a loosely adherent fine powder: this process is termed chalking [61].

The gloss variation is shown in Figure 6. After the first degradation cycle, all the samples have a high gloss retention: their gloss values are practically unchanged. Starting from the second cycle the gloss values decrease: as the gloss is not uniform over the whole surface, the measurements are

affected by high variability. This variability greatly decreases as the gloss stabilizes at very low values. This sharp decrease in gloss is due to the chemical degradation of the coatings, with consequent opacification. The performances of the four samples are very similar to each other, as previously observed in Figure 5. In this case, however, the great change of properties occurs only after the second cycle, while the chemical degradation occurred mainly during the first cycle of exposure to aggressive environments, as highlighted by the FTIR analysis (Figure 5). Since the surface of the samples is not homogeneous and uniform, the measured gloss values are not constant. As a result, high standard deviation values were measured in the second cycle.

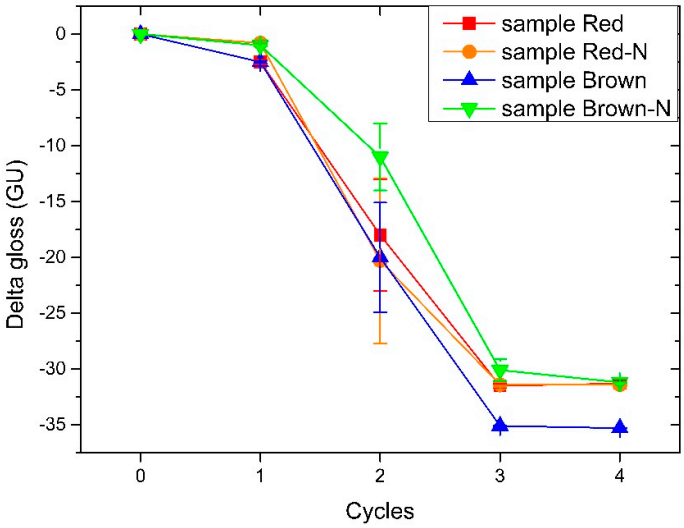

Figure 6. Gloss evolution as a function of the degradation cycles.

The trend of the color variation ΔE_{ab} presented in Figure 7 is pretty different from that of the gloss. The ΔE_{ab} grows uniformly with slopes that depend on the sample. No drops or peaks are observed. The color retention seems to be related to the color itself: the red coatings, in fact, show a faster change of color respect to the brown ones. After the fourth degradation cycle, all the investigated samples show a similar, albeit limited, color change.

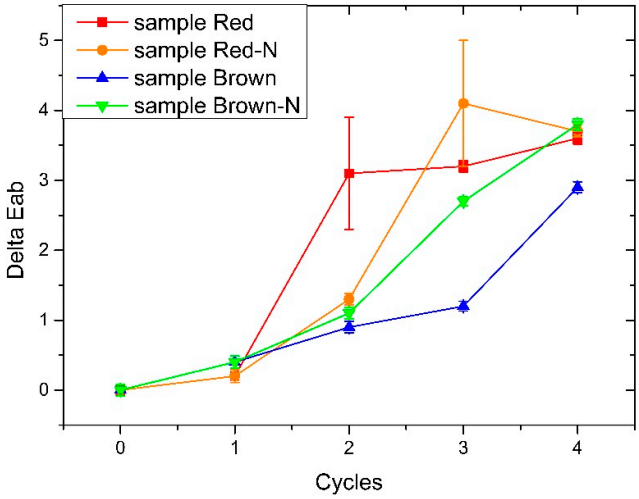

Figure 7. Color difference evolution ΔE_{ab} considering CIELab system as a function of the degradation cycles.

Figure 8 shows the pictures of the two NIR samples, taken as an example, at the initial state and after the fourth degradation cycle. Exposure to aggressive environmental conditions led to the evolution of several corrosion products. These are mainly due to the corrosion of the galvanized surface under the coating: the zinc oxides developed where the sheet was cut, in areas not coated by the paint. The zinc layer oxidized preferentially, protecting the underlying steel.

One of the problems of using coil coatings in many applications is related to the cutting of the sheet which leaves the edges uncovered. These, therefore, are no longer protected either by the galvanizing process or by the paint. The protection of the cut-edges after the installation of the coils would involve additional operations but above all additional costs that may no longer justify the use of coil coatings from an economic point of view. For this reason, there are numerous works that study the corrosion behavior of the coil with the edges uncovered to define the criticality of this aspect [62–67]. In the accelerated tests, therefore, the edges of the samples were not covered, in order to simulate as much as possible the real use of the coil coatings, as previously described.

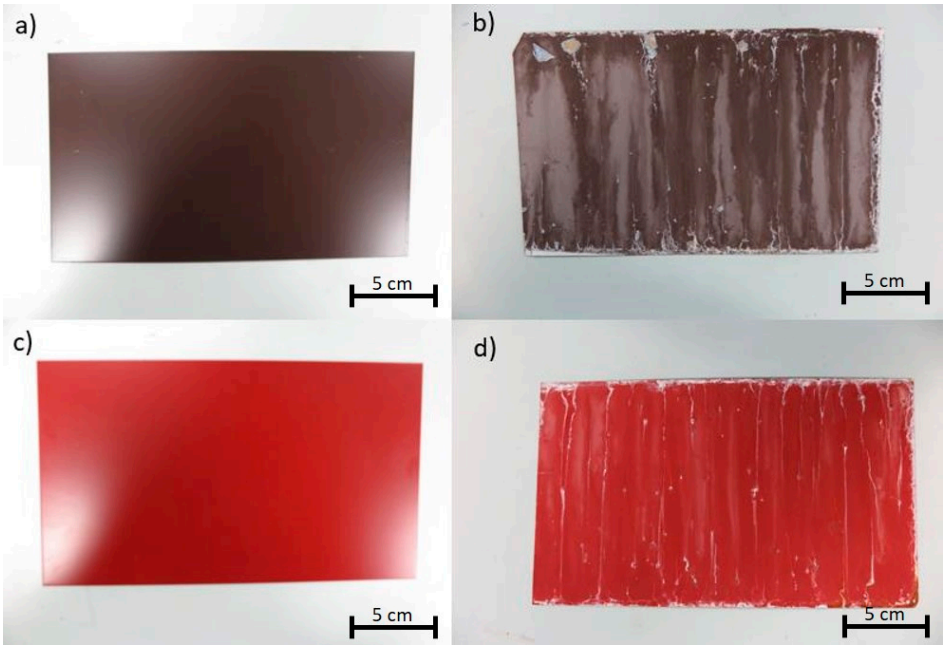

Figure 8. Red-N and Brown-N surfaces at the initial stage (**a**,**c**) and after the fourth degradation cycle (**b**,**d**).

In all cases, at the end of the four degradation cycles, the surface of the samples is covered by many blisters and cracks, as shown in Figure 9. Defects such as those shown in Figures 8 and 9 represent critical points related to the protective properties of the coatings. The physical integrity of the coatings decreases with the degradation cycles. The protection properties expected from roof coatings products are lost as a consequence of exposure in aggressive environments. The performance of the coatings, however, are not influenced by the presence of the NIR pigments, since all four samples showed similar behavior, with the development of defects of the same entity.

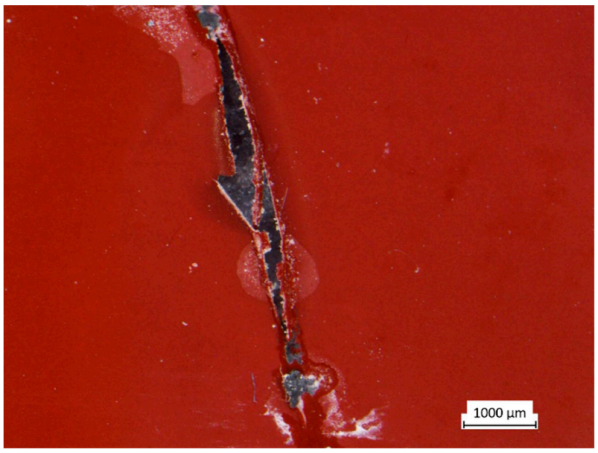

Figure 9. Crack on the surface of sample Red-N after the fourth degradation cycle.

3.2.3. Thermal Evaluation

After having ascertained that a chemical and appearance degradation of the paint has occurred, it was also investigated whether the thermal properties have also been compromised. The thermal performances of the samples were evaluated after each degradation cycle, using the model schematized in Figure 1. The internal temperature is a measure of the flow of heat entering the house: it depends on the reflectivity and emissivity properties of the external topcoat but also on the emissivity of the rear surface of the sample. The same evaluation can be associated with the temperature of the surface facing the IR lamp. If the emissivity of the rear surface is decreased, the heat flux decreases but the temperature of the metal sheet sample increases.

Before subjecting the samples to the degradation cycles, their surface (T_{sup}) and internal (T_{int}) plateau temperatures were measured, as shown in Table 6.

Table 6. Superficial (T_{sup}) and internal (T_{int}) temperatures of the samples before the degradation cycles.

Sample	T_{sup} (°C)	T_{int} (°C)
Red	55.2	38.2
Red-N	54.0	38.2
Brown	72.9	47.6
Brown-N	58.1	38.8

While there are no major performance differences between the two red coatings, the NIR pigments in the brown coating promote the reduction of both the superficial and internal temperature values.

Figure 10 shows the evolution of the plateau temperatures as a function of the degradation cycles.

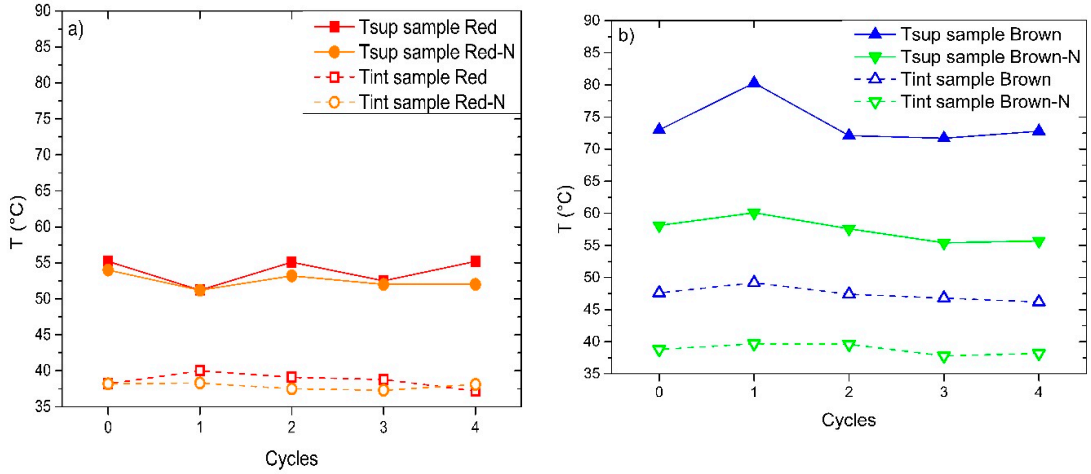

Figure 10. Plateau temperature of (**a**) red coatings and (**b**) brown coatings as a function of degradation cycles.

Comparing the red samples with the brown ones, the latter, being darker in color, have a lower intrinsic reflectivity. Thus, higher temperatures are measured during the test. The addition of NIR pigments, however, greatly improves the reflectance and emissivity properties of the Brown-N coating, whose thermal performances are similar to the red layers.

The thermal behavior of the coatings is not substantially affected by the degradation cycles. Despite a change in gloss and color that occurs after the second exposure cycle, the coatings maintain their initial thermal performance. The severe physical deterioration shown in Figures 8 and 9 is, therefore, not associated with a decrease in the thermal features of these coatings, which offer adequate guarantees as products for roof coatings.

3.2.4. Contact Angle Measurements

Changes in the wettability of the surface can affect the dirt pick up properties of the coating. The wettability of the samples was, therefore, measured before and after the degradation test (fourth cycle). The results are tabulated in Table 7.

Table 7. Contact angle measurements (θ) at initial state ($t = 0$) and after the fourth cycle ($t = 4$ cycles).

Sample	$\theta_{t=0}$ (°)	$\theta_{t=4\ cycles}$ (°)
Red	82.1 ± 1.6	44.8 ± 14.4
Red-N	82.9 ± 2.5	38.4 ± 22.2
Brown	79.5 ± 1.9	44.0 ± 5.0
Brown-N	79.3 ± 1.8	55.7 ± 9.6

The exposure to aggressive environments inevitably led to a decrease in the contact angle, due to the chemical and morphological degradation of the coatings. However, despite the high levels of photooxidation and color change, the Brown-N coating seems to be less affected by the degradation cycles, with final contact angle values higher than the other samples. On the other hand, the results of Table 7 show high standard deviation values: in fact, the wettability was not uniform on the whole surface, probably due to the presence of low surface tension components or contaminants. This great dispersion of results must be taken into consideration when making such measurements.

Finally, Figure 11 shows, as an example, what was observed with the Red-N sample.

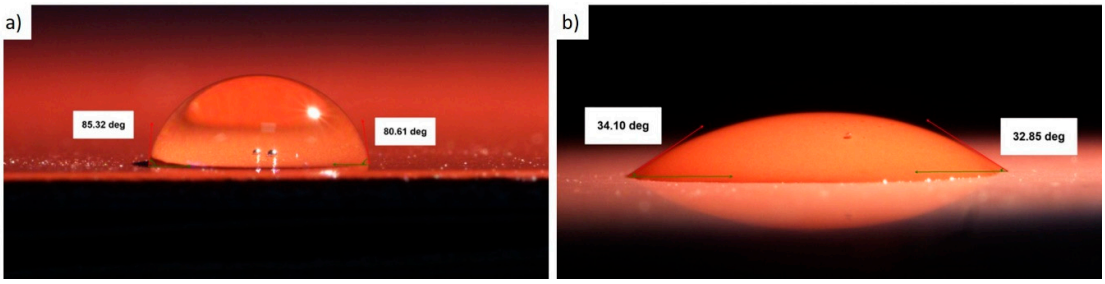

Figure 11. Contact angle measurements of sample Red-N (**a**) before and (**b**) after the degradation cyclic test.

3.3. Effect of Soiling and Weathering

The accelerated soiling and weathering test was carried out following the ASTM D7897/18 [57] standard practice on each sample. The results are summarized in Table 8. The presence of dirt on the surface of the samples does not seem to affect their thermal performance. After washing the coatings, slightly lower temperatures were measured, both internal and external. On the other hand, such minimal differences can also be due to the measurement setup.

Table 8. Comparison of plateau temperatures, both external and internal, between soiled samples and washed samples. ΔT_{ext} and ΔT_{int} are the differences between the soiled samples compared with the washed samples for external and internal plateau temperatures, respectively.

Sample	$T_{ext,wash}$ (°C)	$T_{int,wash}$ (°C)	$T_{ext,soil}$ (°C)	$T_{int,soil}$ (°C)	ΔT_{ext}	ΔT_{int}
Red	54.16	37.81	55.54	38.22	1.38	0.41
Red-N	54.51	36.51	55.02	37.86	0.52	1.36
Brown	74.51	46.43	74.78	46.41	0.19	0.00
Brown-N	55.49	36.61	54.04	36.69	−1.45	0.08
Primer	50.80	32.32	52.42	33.59	1.62	1.27

On the basis of these results, the test was conducted also on a sheet coated with just the primer without the topcoat. This further test was carried out in order to examine how the soiling process affects a light color, as the primer is light gray colored. Differently, an increment of the plateau temperatures is clearly observed in the primer sample. This is probably due to the fact that the dirt, in particular the humic acid and carbon black, decreases the reflectivity of coatings. Since red and brown represent dark colors, they possess low reflectivity in the visible range (11% for red and 7% for brown). As a matter of fact, the study on which the ASTM standard is based [12] takes as a reference a white single-ply membrane.

It is, therefore, deduced that dirt influences the thermal properties of the coatings acting mainly in the field of reflectance of the visible range. Dark-colored coatings, which already possess low intrinsic levels of reflectance in the visible range, such as those studied in this work, therefore, suffer little from these soiling processes.

4. Conclusions

This work aims to characterize and to assess the thermal and degradation performances of different polyester-based organic coil coatings for roofing application, highlighting the differences between the colors (red and brown) and between the standard and NIR-reflective products.

First of all, FTIR measurements have shown a continuous chemical degradation of the coatings following exposure in an aggressive environment, highlighted especially immediately after the first degradation cycle. The brown samples suffered greater degradation phenomena, whose photooxidation seems to be accentuated by the NIR pigments.

After the second cycle, the gloss values tend to decrease, with a consequent change of the color of the investigated coatings. In this case the results do not seem to be influenced by the color of the

coating or by the presence of particular NIR pigments. All the samples, after the fourth degradation cycle, show high defects, cracks and corrosion products.

The thermal performance of the samples does not seem to suffer from degradation cycles and from the defectiveness developed during the exposure in aggressive environments. On the other hand, the thermal properties depend very much on the color of the coating: the brown samples, being darker and less reflective, allow greater absorption of heat flow inside the model used for the thermal characterization tests. The measured temperatures of the Brown-N sample, however, are significantly mitigated thanks to the addition of NIR pigments. Finally, the samples were subjected to soiling and weathering tests, which however did not show significant changes in the thermal performance of the coatings. The dirt in fact seems to mostly influence light-colored layers, with high reflectance in the visible range.

Ultimately, the samples studied in this work represent good products for roof coatings applications: the thermal performances are in fact not influenced by the aging and soiling processes, despite phenomena of chemical degradation, color change and gloss. Furthermore, the presence of NIR pigments, while not radically changing the properties of the red color coating, significantly improves the thermal behavior of dark layers, such as the brown layer.

Author Contributions: Conceptualization, S.R. and D.D.; methodology, D.D. and S.R.; formal analysis, D.D.; data curation, D.D.; writing—original draft preparation, M.C.; writing—review and editing, M.C. and M.F.; supervision, S.R.; project administration, S.R. All authors have read and agreed to the published version of the manuscript.

Funding: This research received no external funding.

Acknowledgments: The authors are grateful to Eng. A. Bonoli from Marcegaglia Carbon Steel (Marina di Ravenna, Italy) for the samples provided.

Conflicts of Interest: The authors declare no conflicts of interest.

References

1. European Commision. Energy Efficiency in Buildings. Available online: https://ec.europa.eu/energy/en/topics/energy-efficiency/ energy-performance-of-buildings (accessed on 15 February 2020).
2. Konstantinidou, C.A.; Lang, W.; Papadopoulos, A.M.; Santamouris, M. Life cycle and life cycle cost implications of integrated phase change materials in office buildings. *Int. J. Energy Res.* **2019**, *43*, 150–166.
3. Mavrakou, T.; Polydoros, A.; Cartalis, C.; Santamouris, M. Recognition of Thermal Hot and Cold Spots in Urban Areas in Support of Mitigation Plans to Counteract Overheating: Application for Athens. *Climate* **2018**, *16*, 1–12.
4. EPA. Heat Island Effect. Available online: https://www.epa.gov/heat- islands (accessed on 8 January 2020).
5. Asimakopoulos, D.N.; Assimakopoulos, V.D. *Energy and Climate in the Urban Built Environment*; Santamouris, M., Ed.; Routledge: London, UK, 2001; doi:10.4324/9781315073774.
6. Gunawardena, K.; Wells, M.; Kershaw, T. Utilizing green and blue space to mitigate urban heat island intensity. *Sci. Total Environ.* **2017**, *584–585*, 1040–1055.
7. Zhang, L.; Deng, Z.; Liang, L.; Zhang, Y.; Meng, Q.; Wang, J.; Santamouris, M. Thermal behavior of a vertical green facade and its impact on the indoor and outdoor thermal environment. *Energy Build.* **2019**, *204*, 109502.
8. Shahmohamadi, P.; Che-Ani, A.I.; Ramly, A.; Maulud, K.N.A.; Mohd-Nor, M.F.I. Reducing urban heat island effects: A systematic review to achieve energy consumption balance. *Int. J. Phys. Sci.* **2010**, *5*, 626–636.
9. Synnefa, A.; Santamouris, M.; Apostolakis, K. On the development, optical properties and thermal performance of cool colored coatings for the urban environment. *Sol. Energy* **2007**, *81*, 488–497.
10. Santamouris, M.; Paraponiaris, K.; Mihalakakou, G. Estimating the ecological footprint of the heat island effect over Athens, Greece. *Clim. Chang.* **2007**, *80*, 265–276, doi:10.1007/s10584-006-9128-0.
11. Santamouris, M.; Cartalis, C.; Synnefa, A.; Kolokotsa, D. On the impact of urban heat island and global warming on the power demand and electricity consumption of buildings—A review. *Energy Build.* **2015**, *98*, 119–124, doi:10.1016/j.enbuild.2014. 09.052.

12. Sleiman, M. Soiling of building envelope surfaces and its effect on solar reflectance—Part II: Development of an accelerated ageing method for roofing materials. *Sol. Energy Mater. Sol. Cells* **2014**, *122*, 271–281.
13. Yang, J.; Kumar, D.I.M.; Pyrgou, A.; Chong, A.; Santamouris, M.; Kolokotsa, D.; Lee, S.E. Green and cool roofs' urban heat island mitigation potential in tropical climate. *Sol. Energy* **2018**, *173*, 597–609.
14. Garshasbi, S.; Santamouris, M. Using advanced thermochromic technologies in the built environment: Recent development and potential to decrease the energy consumption and fight urban overheating. *Sol. Energy Mater. Sol. Cells* **2019**, *91*, 21–32.
15. Anand, P.; Sekhar, C.; Cheong, D.; Santamouris, M.; Kondepudi, S. Occupancy-based zone-level VAV system control implications on thermal comfort, ventilation, indoor air quality and building energy efficiency. *Energy Build.* **2019**, *204*, 109473.
16. Kolokotsa, D.D.; Giannariakis, G.; Gobakisa, K.; Giannarakis, G.; Synnefa, A.; Santamouris, M. Cool roofs and cool pavements application in Acharnes, Greece. *Sustain. Cities Soc.* **2018**, *37*, 466–474.
17. Gao, Q.; Wu, X.; Fan, Y. Solar spectral optical properties of rutile TiO2 coated mica-titania pigments. *Dye. Pigm.* **2014**, *109*, 90–95, doi:10.1016/j.dyepig.2014.04.028.
18. Yang, R.; Han, A.; Ye, M.; Chen, X.; Yuan, L. The influence of Mn/N-codoping on the thermal performance of $ZnAl_2O_4$ as high near-infrared reflective inorganic pigment. *J. Alloys Compd.* **2017**, *696*, 1329–1341.
19. Ecco, L.; Rossi, S.; Fedel, M.; Deflorian, F. Color variation of electrophoretic styrene-acrylic paints under field and accelerated ultraviolet exposure. *Mater. Design* **2017**, *116*, 554–564.
20. Huang, X.; Liu, D.; Li, N.; Wang, J.; Zhang, Z.; Zhong, M. Single novel $Ca_{0.5}Mg_{10.5}(HPO_3)_8(OH)_3F_3$ coating for efficient passive cooling in the natural environment. *Sol. Energy* **2020**, *202*, 164–170.
21. Kim, G.; Song, B.; Park, K. Long-term monitoring for comparison of seasonal effects on cool roofs in humid subtropical climates. *Energy Build.* **2020**, *206*, 109572.
22. Sameera, S.; Vidyadharan, V.; Sasidharan, S.; Gopchandran, K. Nanostructured zinc aluminates: A promising material for cool roof coating. *J. Sci. Adv. Mater. Devices* **2019**, *4*, 524–530.
23. Saber, H.H.; Maref, W. Energy Performance of Cool Roofs Followed by Development of Practical Design Tool. *Front. Energy Res.* **2019**, *7*, 122.
24. Shi, D.; Zhuang, C.; Lin, C.; Zhao, X.; Chen, D.; Gao, Y.; Levinson, R. Effects of natural soiling and weathering on cool roof energy savings for dormitory buildings in Chinese cities with hot summers. *Sol. Energy Mater. Sol. Cells* **2019**, *200*, 110016.
25. Baniassadi, A.; Sailor, D.J.; Ban-Weiss, G.A. Potential energy and climate benefits of super-cool materials as a rooftop strategy. *Urban Clim.* **2019**, *29*, 100495.
26. Lv, J.; Tang, M.; Quan, R.; Chai, Z. Synthesis of solar heat-reflective $ZnTiO_3$ pigments with novel roof cooling effect. *Ceram. Int*. **2019**, *45*, 15768–15771.
27. Ullah, M.; Kim, H.J.; Heo, J.G.; Roh, D.K.; Kim, D.-S. Sodium titanate as an infrared reflective material for cool roof application. *J. Ceram. Process. Res.* **2019**, *20*, 86–91.
28. Hu, J.; Yu, X.B. Adaptive thermochromic roof system: Assessment of performance under different climates. *Energy Build.* **2019**, *192*, 1–14.
29. Qu, J.; Guan, S.; Qin, J.; Zhang, W.; Li, Y.; Zhang, T. Estimates of cooling effect and energy savings for a cool white coating used on the roof of scale model buildings. In *IOP Conference Series: Materials Science and Engineering, Proceedings of the 3rd International Conference on New Material and Chemical Industry, Sanya, China, 17–19 November 2018*; IOP Publishing: Bristol, UK, 2019; Volume 479, p. 012024.
30. Yew, M.C.; Yew, M.K.; Saw, L.H.; Ng, T.C.; Chen, K.P.; Rajkumar, D.; Beh, J.H. Experimental analysis on the active and passive cool roof systems for industrial buildings in Malaysia. *J. Build. Eng.* **2018**, *19*, 134–141.
31. Murguia, C.; Valles, D.; Park, Y.-H.; Kuravi, S. Effect of high aged albedo cool roofs on commercial buildings energy savings in U.S.A. climates. *Int. J. Renew. Energy Res.* **2019**, *9*, 65–72.
32. Uemoto, K.L.; Sato, N.M.; John, V.M. Estimating thermal performance of cool colored paints. *Energy Build.* **2010**, *42*, 17–22.
33. Driel, B.V.; Kooyman, P.; Berg, K.V.; Schmidt-Ott, A.; Dik, J. A quick assessment of the photocatalytic activity of TiO_2 pigments—From lab to conservation studio. *Microchem. J.* **2016**, *126*, 162–171.
34. Seija, R. Bottom-like benefits of prepainted metal. *Finish. Today* **2007**, *83*, 20–23.
35. Bianco, M. The coupled galvanizing and painting line at Marcegaglia Plant. *Metall. Plant Technol. Int.* **2008**, *31*, 62–66.

36. Bianco, M. New Galvanizing Line Coupled with High-Speed Painting Line at Marcegaglia's Ravenna Plant, Italy. In Proceedings of the Iron and Steel Technology Conference (AISTech 2009), St. Louis, MO, USA, 4–7 May 2009.
37. Ecca—Prepainted Metal Site. Available online: https://www.prepaintedmetal.eu/home (accessed on 29 April 2020).
38. Genevay, J.-P. The European coil coatings market. *Eur. Coat. J.* **2008**, *9*, 18–21.
39. Siyab, N.; Tenbusch, S.; Willis, S.; Lowe, C.; Maxted, J. Going Green: Making reality match ambition for sustainable coil coatings. *J. Coat. Technol. Res*. **2016**, *13*, 629–643.
40. Jandel, A.S. Coil-coating branch focussing versatility. *Stahl Eisen* **2000**, *120*, 65–66.
41. Jandel, L. Innovative surface design with coil coatings. *Stahl Eisen* **2006**, *18*, 45–47.
42. Santos, D.; Costa, M.R.; Santos, M.T. Performance of polyester and modified polyester coil coatings exposed in different environments with high UV radiation. *Prog. Org. Coat*. **2007**, *58*, 296–302.
43. Deflorian, F.; Rossi, S.; Fedrizzi, L.; Zanella, C. Comparison of organic coating accelerated tests and natural weathering considering meteorological data. *Prog. Org. Coat*. **2007**, *59*, 244–250.
44. Deflorian, F.; Fedrizzi, L.; Rossi, S. Effects of mechanical deformation on the protection properties of coil coating products. *Corros. Sci.* **2000**, *42*, 1283–1301.
45. Condorcoat NB 100 Complex Oxide Convertion Coating. Available online: https://condoroil.com/docs_skt_imgs/SK_TECH_prod/St-%20Condorcoat%20NB%20100%20Rev.%2003.10%20Inglese.pdf (accessed on 29 April 2020).
46. Condorcoat EC 980: New Chrome Free Pretreatment for Galvanized Steel. Available online: https://www.expometals.net/en-gb/news-page-condoroil-group/condorcoat-ec-980-new-chrome-free-pretreatment-for-galvanized-steel-id12028 (accessed on 29 April 2020).
47. Giannakopoulos, I. The Mechanical Properties of Polyester Based Coil Coatings. Correlations with chemical structure. Ph.D. Thesis, Imperial College, London, UK, 2012.
48. Overview of RAL Classic Colours. Available online: https://www.ral-farben.de/content/anwendung-hilfe/all-ral-colours-names/overview-ral-classic-colours.html (accessed on 16 April 2020).
49. RAL Colours. Available online: https://www.ralcolor.com/ (accessed on 16 April 2020).
50. Detrie, T.; Swiler, D. Infrared Reflecting Complex Inorganic Colored Pigments. In *High Performance Pigments*, 1st ed.; Wiley-VCH: Weinheim, Germany, 2009; Volume 24, pp. 467–487.
51. Bendiganavale, A.; Malshe, V. Infrared Reflective Inorganic Pigments. *Recent Pat. Chem. Eng.* **2008**, *1*, 167–79.
52. *Standard Practice for Operating Fluorescent Light Apparatus for UV Exposure of Nonmetallic Materials*; ASTM G154-06; ASTM International: West Conshohocken, PA, USA, 2006.
53. *Standard Practice for Operating Salt Spray (Fog) Apparatus*; ASTM B117-18; ASTM International: West Conshohocken, PA, USA, 2018.
54. *Standard Test Method for Specular Gloss*; ASTM D523-14(2018); ASTM International: West Conshohocken, PA, USA, 2018
55. Carter, E.C.; Ohno, Y.; Pointer, M.R.; Robertson, A.R.; Seve, R.; Schanda, J.D.; Witt, K. *Colorimetry*, 3rd ed.; CIE 15: Technical Report; Commission Internationale de l'éclairage: Vienna, Austria, 2004.
56. *Standard Practice for Surface Wettability of Coatings, Substrates and Pigments by Advancing Contact Angle Measurement*; ASTM D7334-08; ASTM International: West Conshohocken, PA, USA, 2013.
57. *Standard Practice for Laboratory Soiling and Weathering of Roofing Materials to Simulate Effects of Natural Exposure on Solar Reflectance and Thermal Emittance*; ASTM D7897-18; ASTM International: West Conshohocken, PA, USA, 2018.
58. Talbert, R. Quality Control. In *Paint Technology Handbook*, 1st ed.; CRC Press: Boca Raton, FL, USA, 2008; Volume 11, pp. 184–189.
59. Gerlock, J.L.; Peters, C.A.; Kucherov, A.V.; Misovski, T.; Seubert, C.M.; Carter, R.O.; Nichols, M.E. Testing accelerated weathering tests for appropriate weathering chemistry: Ozone filtered xenon arc. *J. Coat. Technol.* **2003**, *75*, 35–45.
60. Batista, M.A.J.; Moraes, R.P.; Barbosa, J.C.S.; Oliveira, P.C.; Santos, A.M. Effect of the polyester chemical structure on the stability of polyester–melamine coatings when exposed to accelerated weathering. *Prog. Org. Coat*. **2011**, *71*, 265–273.
61. Gheno, G.; Ganzerla, R.; Bortoluzzi, M.; Paganica, R. Accelerated weathering degradation behavior of polyester thermosetting powder coatings. *Prog. Org. Coat.* **2016**, *101*, 90–99.

62. Prosek, T.; Nazarov, A.; Thierry, D. Role of steel and zinc coating thickness in cut edge corrosion of coil coated materials in atmospheric weathering conditions; Part 2: Field data and model. *Prog. Org. Coat.* **2016**, *101*, 45–50.
63. Prosek, T.; Nazarov, A.; Xue, H.B.; Lamaka, S.; Thierry, D. Role of steel and zinc coating thickness in cut edge corrosion of coil coated materials in atmospheric weathering conditions; Part 1: Laboratory study. *Prog. Org. Coat.* **2016**, *99*, 356–364.
64. Marques, A.G.; Izquierdo, J.; Souto, R.M.; Simões, A.M. SECM imaging of the cut edge corrosion of galvanized steel as a function of pH. *Electrochim. Acta* **2015**, *153*, 238–245.
65. Yildiz, R.; Dehri, I. Investigation of the cut-edge corrosion of organically-coated galvanized steel after accelerated atmospheric corrosion test. *Arab. J. Chem.* **2015**, *8*, 821–827.
66. Prosek, T.; Nazarov, A.; Le Gac, A.; Thierry, D. Coil-coated Zn-Mg and Zn-Al-Mg: Effect of climatic parameters on the corrosion at cut edges. *Prog. Org. Coat.* **2015**, *83*, 26–35.
67. McMurray, H.N.; Williams, D.; Worsley, D.A. Cut edge corrosion protection in organically coated galvanised steels using ion exchanged and naturally occurring clay mineral pigments. *ECS Transactions* **2006**, *1*, 153–164.